The Astrophysical Journal, 976:238 (13pp), 2024 December 1 https://doi.org/10.3847/1538-4357/ad83cf

Unlocking Discovery Potential for Decaying Dark Matter and Faint X-Ray Sources with XRISM

Yu Zhou[1], Volodymyr Takhistov[1,2,3,4], and Kazuhisa Mitsuda[1,5]
[1] International Center for Quantum-field Measurement Systems for Studies of the Universe and Particles (QUP, WPI), High Energy Accelerator Research Organization (KEK), Oho 1-1, Tsukuba, Ibaraki 305-0801, Japan; zhouyu@post.kek.jp, vtakhist@post.kek.jp, kmitsuda@post.kek.jp
[2] Theory Center, Institute of Particle and Nuclear Studies (IPNS), High Energy Accelerator Research Organization (KEK), Tsukuba 305-0801, Japan
[3] Graduate University for Advanced Studies (SOKENDAI), 1-1 Oho, Tsukuba, Ibaraki 305-0801, Japan
[4] Kavli Institute for the Physics and Mathematics of the Universe (WPI), The University of Tokyo Institutes for Advanced Study, The University of Tokyo, Kashiwa, Chiba 277-8583, Japan
[5] National Astronomical Observatory of Japan, 2-21-1 Osawa, Mitaka, Tokyo 181-8588, Japan
Received 2024 August 9; revised 2024 October 3; accepted 2024 October 4; published 2024 November 26

Abstract

Astrophysical emission lines arising from particle decays can offer unique insights into the nature of dark matter (DM). Using dedicated simulations with background and foreground modeling, we comprehensively demonstrate that the recently launched X-Ray Imaging and Spectroscopy Mission (XRISM) space telescope with powerful X-ray spectroscopy capabilities is particularly well suited to probe decaying DM, such as sterile neutrinos and axion-like particles, in the mass range of a few to tens of keV. We analyze and map XRISM's DM discovery potential parameter space by considering the Milky Way Galactic DM halo, including establishing an optimal line-of-sight search, as well as dwarf galaxies, where we identify Segue 1 as a remarkably promising target. We demonstrate that with only 100 ks exposure, the XRISM/Resolve instrument is capable of probing the underexplored DM parameter window around a few keV and testing DM couplings with a sensitivity that exceeds by two orders existing Segue 1 limits. Further, we demonstrate that XRISM/Xtend instrument sensitivity enables discovery of the nature of faint astrophysical X-ray sources, especially in Segue 1, which could shed light on star formation history. We discuss implications for decaying DM searches with improved detector energy resolution in future experiments.

Unified Astronomy Thesaurus concepts: X-ray astronomy (1810); Dwarf galaxies (416); Dark matter (353)

1. Introduction

Dark matter (DM) comprises about ∼85% of all the matter in the Universe (see, e.g., G. Bertone et al. 2005 for a review). However, all the knowledge of DM thus far originates only from its gravitational interactions. Unraveling the mysterious nature of DM remains among the most pressing open problems in science.

While DM particles are expected to be long-lived, a multitude of theories suggest that DM can decay with distinct, powerful signatures well suited for indirect DM detection. Especially promising are DM decay processes resulting in monoenergetic photons that can be sensitively distinguished from typical smooth astrophysical backgrounds. Among well-motivated decaying DM candidates are sterile neutrinos and axion-like particles (ALPs).

Sterile (or right-handed) neutrinos, ν_s, have been intimately linked to various puzzles, such as the origin (P. Minkowski 1977; M. Gell-Mann et al. 1979; T. Yanagida 1979) of small observed neutrino masses (Y. Fukuda et al. 1998). We consider sterile neutrinos of mass m_s to mix with active neutrinos ν_a of the standard model with mixing angle $\sin\theta$. Sterile neutrinos constitute a prime warm DM candidate for typical masses around keV (see, e.g., A. Boyarsky et al. 2019), and their radiative decays $\nu_s \to \nu_a + \gamma$ can be efficiently detected through monochromatic X-ray line emission originating from various astrophysical targets. A possible signal has been claimed at 3.5 keV (A. Boyarsky et al. 2014; E. Bulbul et al. 2014) from galaxy cluster observations that could be associated with decays of sterile neutrino DM with $m_s = 7.1$ keV and $\sin^2 2\theta = 5 \times 10^{-11}$, but this has been challenged (e.g., C. Dessert et al. 2020). Other parameter space of decaying sterile neutrinos is also of interest, such as in connection with tensions in measurements of the Hubble parameter (e.g., G. B. Gelmini et al. 2020a, 2021). We consider natural units $c = \hbar = 1$ throughout.

Sensitive searches of decaying keV-mass DM have been carried out using X-ray observations, including the Milky Way's Galactic halo (e.g., N. Sekiya et al. 2016; K. Perez et al. 2017; B. M. Roach et al. 2023; C. Dessert et al. 2024; R. Krivonos et al. 2024), the Perseus galaxy cluster (e.g., T. Tamura et al. 2015; F. A. Aharonian et al. 2017), the Bullet cluster (e.g., S. Riemer-Sørensen et al. 2015), and the Local Group with the Andromeda (M31) galaxy (e.g., S. Horiuchi et al. 2014; K. C. Y. Ng et al. 2019), and can provide stringent tests of DM production mechanisms. Sterile neutrino DM produced via nonresonant active-sterile oscillations via the Dodelson–Widrow mechanism (S. Dodelson & L. M. Widrow 1994) is already strongly constrained as the dominant DM component. However, the allowed sterile neutrino DM parameter space can be significantly modified depending on production, such as when significant lepton asymmetry (X. Shi & G. M. Fuller 1999) or additional neutrino self-interactions (e.g., A. de Gouvea et al. 2020; C. Chichiri et al. 2022; T. Bringmann et al. 2023) are present. Recently, intriguing novel X-ray and gravitational-wave coincidence signatures have been put forth for decaying sterile neutrino DM originating from evaporating early

Universe black holes independently of couplings (M. Chen et al. 2024). We note that sterile neutrinos could themselves serve as excellent probes of early cosmological epochs (G. B. Gelmini et al. 2019, 2020a, 2020b, 2020c; C. Chichiri et al. 2022).

ALPs constitute another motivated decaying keV-scale DM candidate (e.g., T. Higaki et al. 2014; J. Jaeckel et al. 2014). A prominent feature of pseudoscalar ALPs is their coupling to photons $(1/4)g_{a\gamma\gamma}F^{\mu\nu}\tilde{F}_{\mu\nu}$. Decays to photons of ALP DM $a \to 2\gamma$ have been associated with the claimed putative 3.5 keV signal for ALP mass $m_a = 7.1$ keV and coupling $g_{a\gamma\gamma} \sim$ few $\times 10^{-18}$ GeV^{-1} (e.g., T. Higaki et al. 2014; J. Jaeckel et al. 2014). Such ALPs constituting cold DM can be produced via a misalignment mechanism in the early Universe (e.g., P. Arias et al. 2012). For strongly coupled keV-scale ALPs, even subdominant irreducible DM density contributions can be detected in X-rays (K. Langhoff et al. 2022). Prominent X-ray signatures can also arise from relativistic ALPs produced in various scenarios from transient sources contributing to the diffuse axion background (J. Eby & V. Takhistov 2024).

In this work, we comprehensively analyze the discovery potential of keV-scale decaying DM with the Resolve instrument on board the X-Ray Imaging and Spectroscopy Mission (XRISM; M. Tashiro et al. 2018; XRISM Science Team 2020) that was successfully launched on 2023 September 7 and is a successor of the ASTRO-H (Hitomi) mission that operated in 2016 and prematurely concluded observations. The high-energy-resolution X-ray spectroscopy with Resolve using an X-ray microcalorimeter array (FWHM $\sim$ 5 eV) offers unique opportunities to probe astrophysical source emission as well as decaying DM, while Xtend, the wide-field CCD-resolution spectroscopy (FWHM $\sim$ 200 eV), provides monitor observations of the sky wider than Resolve. Early preliminary estimates of XRISM/Resolve sensitivity have been discussed for dwarf galaxies (DGs; S. Ando et al. 2021) and the Galactic halo[6] (C. Dessert et al. 2024). Our analysis significantly expands on and improves multiple key aspects of chart discovery potential for XRISM, including using dedicated simulations, spectral analyses with background and foreground modeling, as well as consideration of multiple distinct targets to optimize the search for decaying DM. More so, we discuss opportunities for XRISM to detect faint astrophysical X-ray sources challenging to test otherwise.

2. Decaying DM

For keV-scale sterile neutrino DM, the dominant decays are $\nu_s \to \nu_a + \gamma$, resulting in monochromatic X-ray photons with energies $E_\gamma = m_s/2$. The channel decay rate is (R. Shrock 1974; P. B. Pal & L. Wolfenstein 1982)

$$\Gamma_{\nu_s \to \gamma\nu_a} = 1.38 \times 10^{-32} \left(\frac{\sin^2 2\theta}{10^{-10}}\right)\left(\frac{m_s}{1\ \mathrm{keV}}\right)^5 \mathrm{s}^{-1}, \quad (1)$$

considering Majorana sterile neutrinos. For keV-scale pseudoscalar ALPs, $m_a \ll m_e$ compared to electron mass m_e, and the decays proceed via $a \to 2\gamma$. Neglecting loop contributions from ALP–electron couplings, the rate is

$$\Gamma_{a \to \gamma\gamma} = 7.56 \times 10^{-31} \left(\frac{g_{a\gamma\gamma}}{10^{-17}\ \mathrm{GeV}^{-1}}\right)^2 \left(\frac{m_a}{1\ \mathrm{keV}}\right)^3 \mathrm{s}^{-1}. \quad (2)$$

[6] In C. Dessert et al. (2024), XRISM projections were obtained using observed background rates from Hitomi and considering only an open GV.

The DM lifetime $\tau = 1/\Gamma$ can be directly compared to the age of the Universe. Note that decaying DM lifetime interpretation differs by a factor of 2 between sterile neutrinos and ALPs due to additional photon emission.

2.1. Galactic Halo

DM accumulates around primordial overdense regions to form halo and subhalo structures under gravitational collapse. The DM halo of the Milky Way provides a unique cosmic laboratory to probe the particle nature of DM. Assuming that the collisionless DM species are in gravitational equilibrium with the gravitational potential of the Galactic DM halo, even though the photons produced by DM decays in our scenario are monochromatic, the resulting line signals are broadened due to Doppler broadening from the DM velocity dispersion.

However, the Galactic hot gaseous halo contributes a photon background whose spatial distribution differs from that of the DM. Therefore, there exist optimal lines of sight where the contribution of DM signals to the photon background is maximized. In our analysis, we compute the ratio of the two halo components and illustrate the optimized region for DM detection.

We model the DM density distribution of the Galactic DM halo using a Navarro–Frenk–White (NFW) profile (J. F. Navarro et al. 1996),

$$\rho_{\mathrm{DM}}(r) = \frac{\rho_s}{(r/r_s)(1 + r/r_s)^2}, \quad (3)$$

with $\rho_s = 6.6 \times 10^6\ M_\odot\ \mathrm{kpc}^{-3}$ and $r_s = 19.1$ kpc. We can also consider a more general form of the DM profile, $\rho_{\mathrm{DM}}(r) = \rho_0 (r/r_s)^{-\gamma}(1 + (r/r_s)^\alpha)^{(\gamma-\beta)/\alpha}$, where $(\alpha, \beta, \gamma) = (1, 3, 1/2)$ represents a more weakly cusped DM halo, and $(\alpha, \beta, \gamma) = (2, 5, 0)$ represents a more cored DM halo (Plummer model). We have verified that the Doppler broadening of the signal line varies by no more than $\mathcal{O}(1)\%$ for different choices of considered DM profiles. We have also confirmed that the impact of the DM profile on the final sensitivity forecast results is not significant.

Finite velocity dispersion of the Milky Way DM in the Galactic frame will result in Doppler broadening,

$$f(E, r) = \frac{4}{m_s} \frac{\int_0^\infty ds \rho_{\mathrm{DM}}(r) f(v(E), r)}{\int_0^\infty ds \rho_{\mathrm{DM}}(r)}, \quad (4)$$

where $f(v(E), r)$ is the DM velocity distribution projected along the line of sight under the assumption of a homogeneous and isotropic DM velocity distribution for a collisionless DM species in gravitational equilibrium with a gravitational potential (W. Dehnen et al. 2006)

$$f(v, r) = \frac{e^{-v^2/v_0(r)^2}}{\sqrt{\pi} v_0(r)}, \quad (5)$$

where $v_0(r)^2 = 2V_c^2(r)/(\gamma - 2\alpha)$, $V_c^2(r) = GM_{\mathrm{tot}}(r)/r$, with G being the gravitational constant. Here, V_c is the circular velocity as a function of the radius r, with $M_{\mathrm{tot}}(r)$ being the mass enclosed within the radius r. The coefficients α and γ are defined by $\alpha = r\partial_r V_c(r)/V_c(r)$, $\gamma = -r\partial_r \rho_{\mathrm{DM}}(r)/\rho_{\mathrm{DM}}(r)$, with $\rho_{\mathrm{DM}}(r)$ the DM density profile as a function of distance from the Galaxy center. We implement velocity distribution by

solving Equation (5) assuming the DM distribution of Equation (3) for mass enclosed at radius r. We have verified instead that an approximately constant velocity distribution of $v_0 = 220\,\mathrm{km\,s^{-1}}$ everywhere in the Galaxy following circular velocity curves (A.-C. Eilers et al. 2019) does not significantly affect our results.

The Doppler broadening of the signal line due to the Galactic DM halo depends on the line of sight and approximately scales with the energy $\sigma \sim 5 \times 10^{-4} E$. For DM mass around 7 keV, the FWHM of the signal line driven by DM halo Doppler broadening is found to be around 4 eV.

Observations have suggested that the Galactic hot gaseous halo has a vertical exponential dependence on the distance away from the Galactic plane, with a temperature scale height of $\sim$1.4 kpc, a density scale height of $\sim$2.8 kpc, and a temperature and density at the Galactic plane $T_0 = 3.6 \times 10^6\,\mathrm{K}$ and $\rho_0 = 1.4 \times 10^{-3}\,\mathrm{cm^{-3}}$ (Y. Yao et al. 2009). We numerically compute the photon surface brightness map according to the Galactic disk model for each line of sight and integrate the emission in the Galactic halo up to 100 kpc. The emissivity of the halo plasma is computed using the APEC code assuming solar abundance of the gas (E. Anders & N. Grevesse 1989). Assuming a sterile neutrino mass $m_a = 7.1$ keV and a sterile-active mixing angle $\sin^2(2\theta) = 10^{-6}$, we create a forecast map of the DM emission surface brightness map and calculate the DM-to-gas surface brightness ratio for all lines of sight, as shown in Figure 1.

2.2. DGs

DGs are the most DM-dominated systems with low quantities of photon emission, which marks them as pristine targets for exploring indirect DM signatures like decays. Further enhancement of DM signals can be expected if appropriate lines of sight are selected where both DG and Galactic DM halo contributions are combined. Given that the mass-to-light ratio M/L and spatial extension vary among galaxies, particular DGs constitute preferred targets for specific energy bands and observing telescopes. As we discuss, among various DGs, Segue 1 is an optimal target for a decaying DM search by XRISM.

To identify favorable DG targets for a decaying DM search, we consider mass-to-light and D-factor ratios as summarized in Figure 2. The mass-to-light ratio M/L within the 3D half-light radius $r_{1/2}$ and the total V-band luminosity L have been analyzed for various DGs (K. H. Cook et al. 1999; M. Geha et al. 2006, 2010; A. W. McConnachie 2012; D. Crnojevic et al. 2014; G. Torrealba et al. 2016; L. Cicuéndez et al. 2018; S. E. Koposov et al. 2018; R. R. Muñoz et al. 2018; M. L. M. Collins et al. 2020, 2021; C. R. Higgs & A. W. McConnachie 2021; A. P. Ji et al. 2021; G. Battaglia et al. 2022). Considering the dynamical mass measured from stellar motion $M_{\rm dyn}$, one can obtain a dynamical mass-to-light ratio within the half-light radius $M/L \equiv M_{\rm dyn}(r_{1/2})/(L/2)$. The majority of the DGs are found to have $M/L \gtrsim 10$, with M/L tending to increase at lower L. Therefore, lower-luminosity DGs are more dominated by the DM in mass.

The D-factor accounts for the distribution of DM in an astrophysical system to determine the strength of the emission signal from decaying DM,

$$D_{\rm DG} = \int_{\Delta\Omega} d\Omega \int dl \rho_{\rm DM}(r(l, \Omega)), \tag{6}$$

where Ω is the solid angle of the chosen field of view and l is the distance along the line of sight. The D-factor ratio of the Milky Way to a given DG can be found from

$$R_{D_{\rm MW}} = \frac{D_{\rm MW}}{D_{\rm MW} + D_{\rm DG}}. \tag{7}$$

This characterizes how the DG DM emission is enhanced compared to the DM signal stemming from the Galactic DM halo (see, e.g., S. Ando et al. 2021). A smaller $R_{D_{\rm MW}}$ indicates more significant DG DM signal enhancement compared to the Milky Way.

In Figure 2, we display D-factor ratio versus M/L ratio. The DGs with the highest $R_{D_{\rm MW}}$ values are Segue 1 and Ursa Major II, having $R_{D_{\rm MW}} = 0.56$ and 0.54, respectively. DGs with the highest M/L ratios and smallest $R_{D_{\rm MW}}$ values constitute particularly favorable targets for a decaying DM search.

Other considerations further indicate that DG Segue 1 is an especially favorable target for our analysis. Taking into account XRISM/Resolve capabilities, which can only observe a very limited field of view ($\sim 2.9 \times 2.9\,\mathrm{arcmin^2}$); half-light radius or DM concentration of the DG are other essential factors for optimal target selection. Segue 1 has a small estimated half-light radius of $\sim 4\farcm3$, ideally matching the XRISM/Resolve field of view. More so, Segue 1 DG has a favorable sky location such that the DM-to-gas surface brightness ratio is relatively high, but it is still far from the Galactic center on the sky map, meaning that it is less affected by the photon contamination from the Galactic hot gaseous halo and gas bubble identified by eROSITA (P. Predehl et al. 2020; A. Gupta et al. 2023; T. Liu et al. 2024).

2.3. Segue 1

Segue 1 is the least luminous of the ultrafaint DGs discovered around the Milky Way. With a mass-to-light ratio considering a V-band luminosity of $M/L_V = 2440^{+1580}_{-1775}$, this DG is found to be DM-dominated at a high significance (M. Geha et al. 2009). The mean heliocentric recession velocity of $206 \pm 1.3\,\mathrm{km\,s^{-1}}$ is measured from 24 stars identified as members of the DG, and the internal velocity dispersion is measured for $4.3 \pm 1.2\,\mathrm{km\,s^{-1}}$ (M. Geha et al. 2009). The DM distribution of the Segue 1 DG is calculated based on the spherical NFW profile. We adopt the D-factor within a $5'$ radius, $9.94 \times 10^{16}\,\mathrm{GeV\,cm^{-2}}$, according to the value in Figure 6 in N. W. Evans et al. (2016). Previously, Segue 1 constraints on sterile neutrino decaying DM were obtained using data from a short $\sim$5 ks X-ray observation period by the Swift telescope (N. Mirabal 2010). As we demonstrate, XRISM can dramatically improve on these results.

Stellar chemical analyses also appear to indicate that Segue 1 remains as a fossil galaxy that might have only experienced a single star formation activity phase (A. Frebel et al. 2014). Hence, besides DM, discovery opportunities of faint X-ray binary sources in Segue 1 that could potentially relay key information about the early epoch of star formation also make it an attractive target source for deep observations with sensitive detectors.

The emission spectrum contributions of decaying DM χ from a DG and the Galactic DM halo along the line of sight can

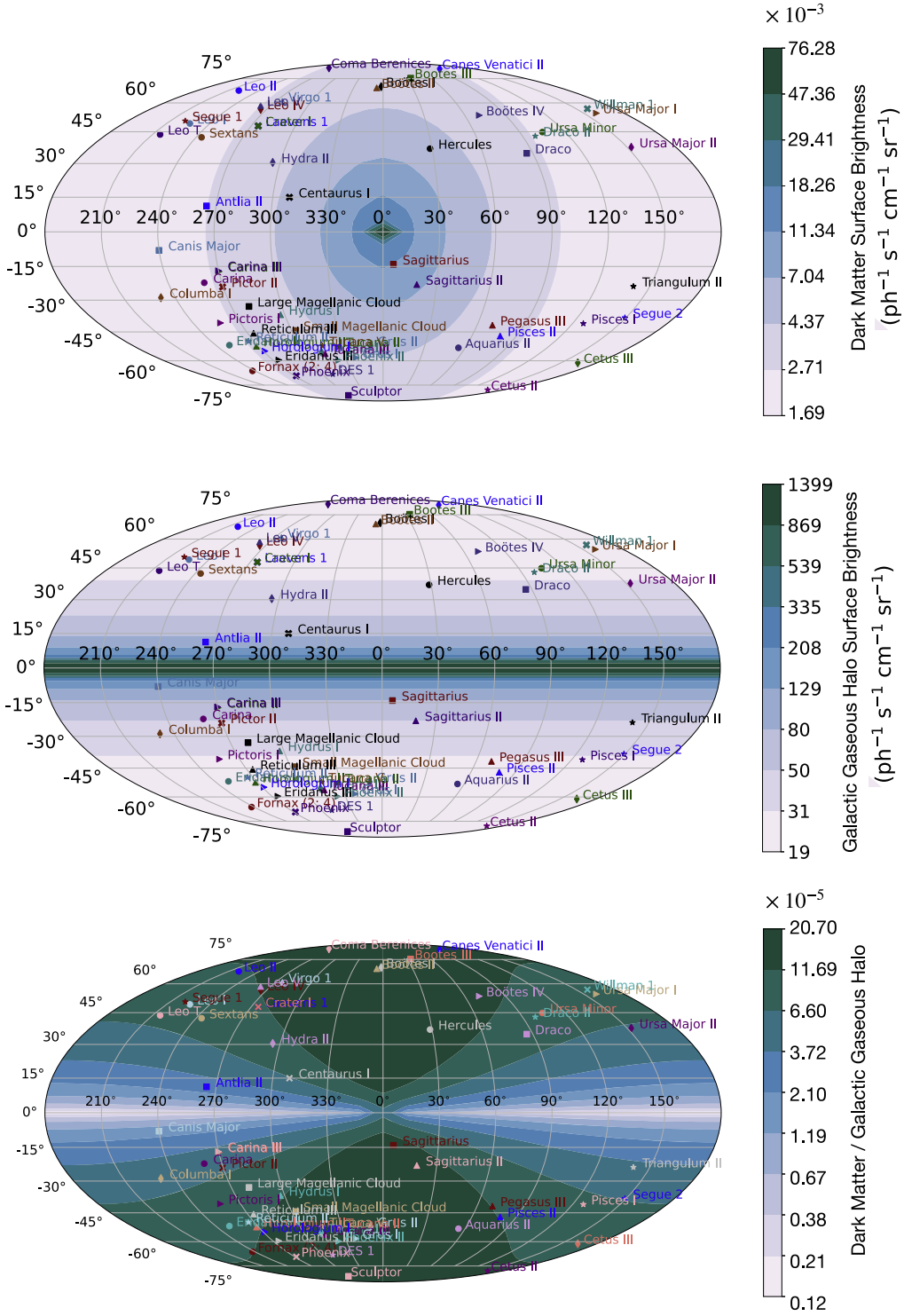

Figure 1. All-sky emission maps plotted in Galactic coordinates, along with reference positions of DGs. (Top) The DM surface brightness distribution assuming that sterile neutrinos constitute all of the DM abundance in the Milky Way Galactic DM halo. (Center) The Galactic hot gaseous halo distribution assuming a disk profile. (Bottom) Map of the ratio of DM to hot gas surface brightness. Note that in the center and bottom figures, only X-ray emission from the hot halo gas is displayed. Selection of optimal observation directions requires proper consideration of X-ray emission from various bright sources, such as the north polar spur (e.g., S. L. Snowden et al. 1997).

be modeled as

$$\frac{d\phi}{dE} = \frac{\Gamma_\chi}{4\pi m_\chi}\left(\frac{dN_{\rm dec}}{dE}\bigg|_{\rm DG} D_{\rm DG} + \frac{dN_{\rm dec}}{dE}\bigg|_{\rm MW} D_{\rm MW}\right). \quad (8)$$

Here, $dN_{\rm dec}/dE$ is the DM decay energy spectrum. Without taking into account Doppler shift or broadening effects, it is just a delta function centered at monochromatic energy $E = m_\chi/2$. In Figure 3, we display the line profile emission

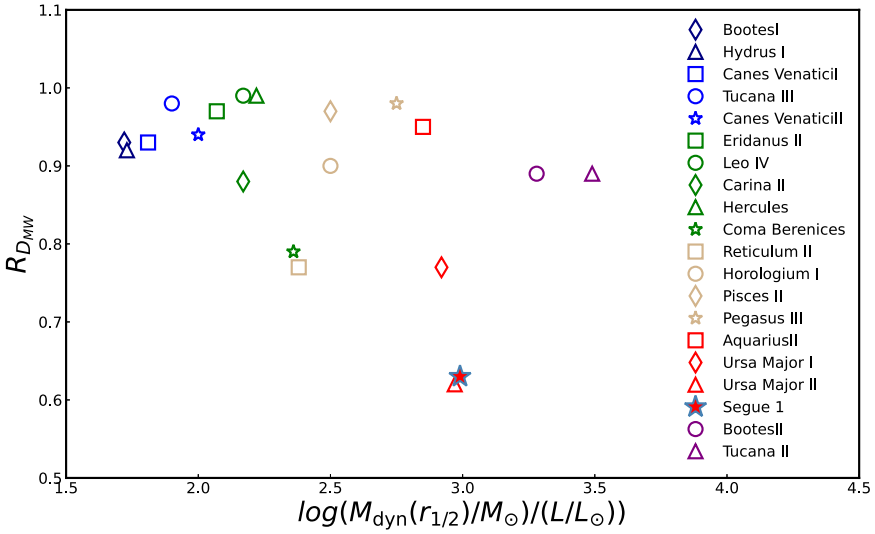

Figure 2. Distribution of the D-factor ratio $R_{D_{\rm MW}}$ of the Milky Way DM halo D-factor $D_{\rm MW}$ along the line of sight to the sum of the D-factor including the $D_{\rm DG}$ of the DG itself as a function of the dynamical mass-to-light ratio within the half-light radius (M/L) in the V band and normalized to the solar mass $M_\odot$ and solar luminosity $L_\odot$. The DGs with higher M/L ratios and lower $R_{D_{\rm MW}}$ constitute particularly favorable targets for a decaying DM search.

of the DM signal from Segue 1 consisting of a redshifted line broadened according to the internal velocity dispersion of Segue 1 superimposed on top of the Galactic DM emission contribution with line width dominated by a Doppler broadening of more than $\sim$4 eV, assuming a DM mass of $m_\chi = 7.2$ keV.

As we demonstrate in Figure 3, the Segue 1 DM signal features could be well distinguished with high energy resolution and statistics observations from atomic signals whose energy distribution is subject to the Voigt profile. The Voigt profile of an atomic line is determined by the transition rate between the energy levels and the thermal temperature of the emitter,

$$V(E, \sigma, \gamma) = \int_{-\infty}^{+\infty} G(E', \sigma) L(E - E', \gamma) dE', \qquad (9)$$

where $G(E, \sigma)$ is a Gaussian distribution of energy E with a width of $\sigma = E\sqrt{2kT/m_{\rm ion} + v_{\rm turb}^2}$ characterizing the thermal broadening due to the gas motion, and $L(E, \gamma)$ is the Lorentzian profile $L(x, \gamma) = \gamma/(\pi(\gamma^2 + x^2))$ with $\gamma = \nu$ being the transition rate frequency. Here, for the atomic line profile shown in Figure 3, we consider reference parameters corresponding to common properties of the hot gases in the Milky Way halo with the temperature of the hot gas $T = 10^7$ K (S. Nakashima et al. 2018); turbulence velocity $v_{\rm turb} = 100\,{\rm km\,s^{-1}}$ (Y. Li & J. Bregman 2017); ion mass $m_{\rm ion} = 39.098 m_p$, with m_p being the proton mass; and a transition rate of $\nu = 3.43 \times 10^{14}$ Hz. The choice of atomic transition parameters is referred to the atomic database `ATOMDB(version 3.0.9)`[7] but assigned with fictitious values. The ion mass has assumed the mass of potassium, and the transition rate is close but not equal to Ar XVII (level $1 \rightarrow 7$, $\nu = 1.09 \times 10^{14}$ Hz).

3. Foreground and Background Emission

In our analysis, we model background and foreground emission by accounting for the following major contributions as shown in Figure 4. In Figure 1, we display the all-sky map of the Galactic gas halo.

1. *Local hot bubble (LHB) and solar-wind charge exchange (SWCX).* The LHB has been discovered around the solar system neighborhood with an irregular size of approximately $\sim$200 pc using observations of an intense diffuse soft X-ray emission coupled with the fact that the solar neighborhood is almost completely devoid of cold gas, leading to a picture of a "local cavity" filled with hot gases (D. McCammon & W. T. Sanders 1990; S. L. Snowden 1993; A. Farhang et al. 2019). We use the collisionally ionized diffuse gas emission spectrum (APEC) to model the LHB. We adopt the temperature corresponding to an average number 61.275 eV of the fitted `APEC` temperature to Suzaku blank-sky X-ray background data sets (Y. Zhou et al. 2022). The surface brightness of the LHB is also set to an average value of the observed Suzaku X-ray background, 165.981 ph s^{-1} cm^{-2} sr^{-1}. Since the LHB emission is considered as local around our solar system, no Galactic absorption from the interstellar medium (ISM) is applied to this component. Due to limitations of the energy resolving power of CCD detectors, the nonthermal line contributions from the SWCX process cannot be distinguished from the LHB component. Therefore, the model of LHB consisting of average parameter values as inferred from Suzaku background observations already includes the impact from SWCX.
2. *Galactic gaseous halo.* Galactic stellar formation processes can eject hot gases into the surrounding environment so that hot gases accumulate near the Galactic plane to form a disk (Y. Yao et al. 2009, 2012; T. Hagihara et al. 2010; K. Sakai et al. 2014). Alternatively, shock heating driven by the DM core collapse can heat the baryons into a warm-hot phase to several million K inside the DM halo (T. Fang et al. 2013). Diffuse hot gas permeating the Galactic DM halo exists in the form of an optically thin thermal plasma, of which we modeled the X-ray emission with the `APEC` model in the XSPEC software (K. A. Arnaud 1996), assuming an average

[7] http://www.atomdb.org/Webguide/webguide.php

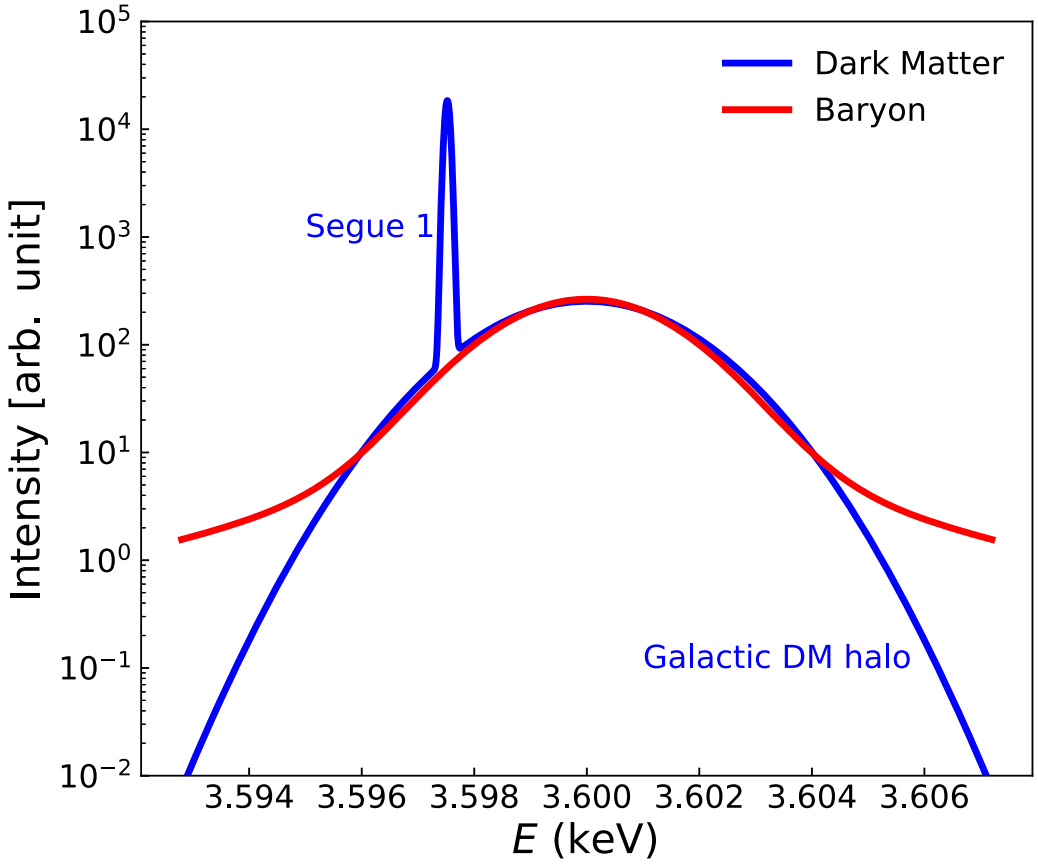

Figure 3. Comparison between the decaying DM signal and the atomic emission from the Segue 1 DG along the line of sight assuming $m_s = 7.1$ keV, highlighting features that can be distinguished by a detector with an appropriate energy resolution. (Blue) Combined decaying DM signal as observed from the Segue 1 DG along the line of sight. The narrow line originates from the Segue 1 DM halo, and the broadened line originates from the Galactic DM halo within the telescope field of view. (Red) Voigt profile presenting a hypothetical atomic emission line from the Galactic hot gaseous halo. Assumed relevant parameters such as turbulence velocity, atomic number, and the transition rate of atomic decays are described in Section 2.3.

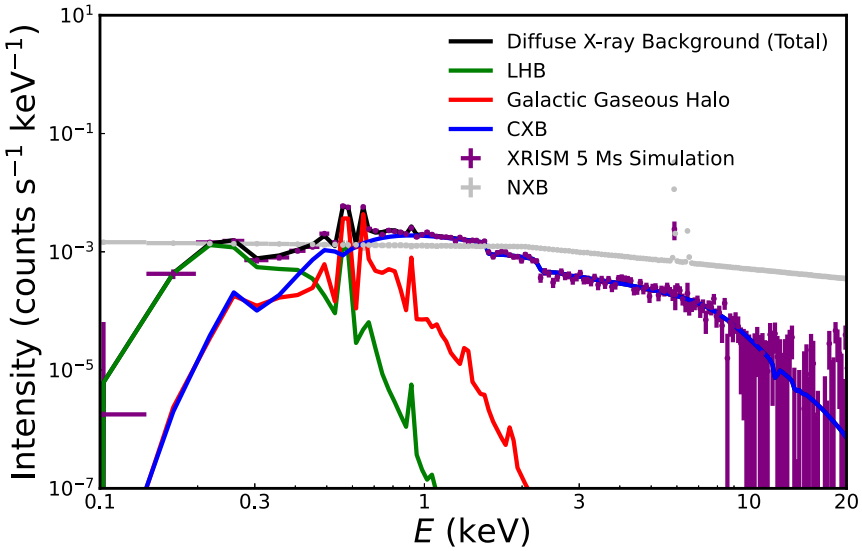

Figure 4. Simulation of XRISM/Resolve. X-ray background showcasing contributing components, considering 5 Ms exposure. Total diffuse X-ray background emission (black) including the LHB, Galactic hot gaseous halo, and CXB, LHB model used in simulation (green), Galactic hot gaseous halo model used in simulation (red), CXB model used in simulation (blue), simulated energy spectrum of the total diffuse X-ray background using XRISM/Resolve response (purple), the non-X-ray background energy spectrum used in the simulation (gray).

temperature of 0.178 keV and an average surface brightness of 6.24 ph s^{-1} cm^{-2} sr^{-1} according to the earlier Suzaku X-ray background analysis by some of us (Y. Zhou et al. 2022). We use the `TBabs` model of XSPEC to account for the Galactic foreground ISM absorption, with the neutral hydrogen column density assumed to the median value considering all Suzaku background observations, i.e., $n_{\rm H} = 1.8 \times 10^{20}$ cm^{-2}.

3. *Extragalactic cosmic X-ray background (CXB).* The predominant contributions to the X-ray background above 2 keV are expected to originate from the distant active galactic nuclei (AGN) and galaxies. We make use of a double broken power law to model CXB emission,

$$\begin{cases} KE^{-\Gamma_1} & \text{if } E \leqslant E_{\rm break} \\ KE_{\rm break}^{\Gamma_2-\Gamma_1}(E/1{\rm keV})^{-\Gamma_2} & \text{if } E > E_{\rm break} \end{cases}, \quad (10)$$

where K is the normalization and we take the photon indices fixed at $\Gamma_1 = 1.96$ and $\Gamma_2 = 1.54$ below the break-point energy $E_{\rm break} = 1.2$ keV and $\Gamma_{1,2} = 1.4$ above $E_{\rm break}$ (T. Yoshino et al. 2009). The normalizations of the broken power-law components are set to 3.7 and 5.7 ph s^{-1} cm^{-2} keV^{-1} sr^{-1} at 1 keV, according to the average normalization value fitted for the Suzaku X-ray background (Y. Zhou et al. 2022). We use `TBabs` to model the Galactic foreground ISM absorption with the same neutral hydrogen column density as described previously. In principle, the unresolved CXB surface brightness could vary among observations taken with different angular resolution and exposure time. The CXB intensity assumed for this work, which is obtained from the Suzaku background, is in agreement with the full CXB intensity measured by the Chandra COSMOS legacy survey within 5% in 0.3–10.0 keV and within 12% in 2–10 keV (N. Cappelluti et al. 2017). N. Cappelluti et al. (2017) have also compared the total unfolded CXB spectrum with other previous observations and illustrate the consistency among Chandra, Swift, ROSAT-ASCA, Integral, and RXTE results with a discrepancy level no larger than 20%.

4. *Faint X-ray binaries in Segue 1.* The eROSITA all-sky survey point-source catalog (A. Merloni et al. 2024) suggests that in the 0.5–2 keV range, there is no significant detection of X-ray point-source emission originating from the central region of the Segue 1 DG in the field of view of XRISM/Resolve. Hence, this is a particularly well-suited target for a DM signal search using XRISM. However, there could exist faint X-ray sources with emission below the eROSITA all-sky survey flux threshold of $F_{0.5-2\,\rm keV} = 5 \times 10^{-14}$ erg s^{-1} cm^{-2} that are in XRSIM's field of view. Assuming that the flux of such a faint source is at the limit probed by eROSITA, we would expect ∼140 counts if observed with XRISM/Xtend for 100 ks exposure time. Given that the energy spectrum of the X-ray binary system is a continuum, the contribution of such faint sources will still be less dominant than the total diffuse X-ray background and the non-X-ray background. Therefore, we can conclude that the Segue 1 DM sensitivity reach is not expected to be significantly degraded due to the unknown faint point-source contamination.
5. *Non-X-ray background.* Energetic particles, mainly protons originating from space or solar activity, can excite secondary photons inside the telescope and contribute a considerable amount of background in the observed energy spectrum (N. Tawa et al. 2008). We simulate a non-X-ray background of XRISM's Resolve spectrometer using dedicated calibration input *resolve_h5ev_2019a_rslnxb.pha*. The resulting count rate of ∼0.06 counts s^{-1} cm^{-2} is consistent with the orbit-averaged data collected by Hitomi/SXS NXB that gives ∼0.04 counts s^{-1} cm^{-2} in the energy range of 0.3–12 keV (C. A. Kilbourne et al. 2018).

4. DM Discovery Reach

4.1. Observation Target Systems

We consider three astrophysical observation target systems and construct DM signal models for them to identify the DM discovery reach sensitivity.

1. *Average random Galactic DM halo lines of sight.* The DM surface brightness is averaged for the Galactic DM halo across the sky (longitude $l = 0°$–$360°$ and latitude $b = 0°$–$90°$) in the model. We configure the temperature and the surface brightness of the Galactic foreground considering the average values obtained from the Suzaku X-ray background analysis.
2. *Optimized Galactic DM halo line of sight.* From the DM-to-gas surface brightness ratio map shown in Figure 1, we have computed that an optimized line of sight exists at $l = 0°$, $b = 40°$, where the DM-to-gas surface brightness ratio reaches maximum. However, the ROSAT hot gas map at 3/4 keV (S. L. Snowden et al. 1997) and the eROSITA all-sky map suggest that a significant amount of hot bubble (i.e., "eROSITA bubble") emission contaminates this region (P. Predehl et al. 2020; A. Gupta et al. 2023; T. Liu et al. 2024). This introduces additional complexity and can obfuscate DM signals in data analysis. Thus, by exploiting the information from both the DM-to-gas surface brightness ratio map and the observed 0.75 keV hot gas map, we have identified a secondary favorable line of sight for a DM search at $l = 330°$, $b = 60°$, where the DM-to-gas surface brightness ratio is significant and photon emission from the eROSITA bubble is low. We compute the DM surface brightness, Doppler broadening, and the surface brightness of the Galactic hot gaseous halo by the disk model specifically for this line of sight and use those parameters in the X-ray background spectrum simulations as well as fit.
3. *Line of sight toward Segue 1.* The DM signal emission originating from the line of sight chosen toward Segue 1 consists of two components. One is from the DM of the DG itself and the other from the Galactic DM halo along the line of sight, as described by Equation (8). In our analysis, we have assumed that the DM associated with Segue 1 possesses the same recession velocity and velocity dispersion as indicated by stars (M. Geha et al. 2009). Thus, we have applied a Doppler redshift of ∼0.7% relative to the rest-frame energy and a Doppler broadening of ∼0.5 eV to the line signal from Segue 1.

4.2. Simulations

The XRISM space telescope observatory is equipped with two detectors, Resolve and Xtend, adopting X-ray microcalorimeter and CCD technology, respectively. The X-ray microcalorimeter XRISM/Resolve covers a field of view of 2.9×2.9 arcmin^2 and an energy band of 0.3–12 keV.

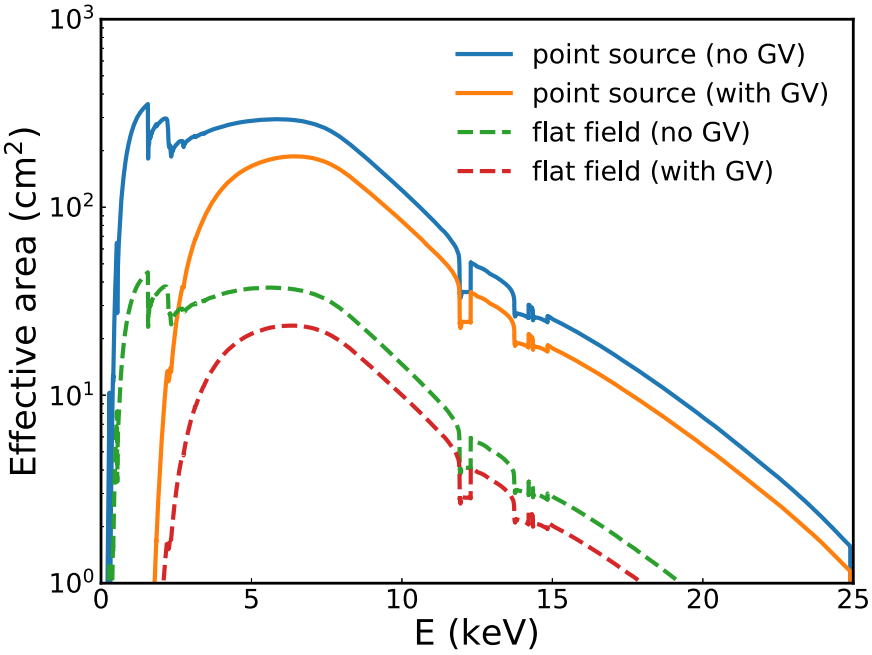

Figure 5. Effective area response of XRISM/Resolve for point sources and flat fields assuming a 5′ radius sky, considering the condition that the GV is open or closed.

XRISM/Resolve has an effective area of $>210\,\mathrm{cm}^2$ at 6 keV and an absolute energy scale of <2 eV. The unprecedented energy resolution of XRISM/Resolve facilitates very high sensitivity for DM signal detection. On the other hand, XRISM/Xtend has a field of view larger than $300\,\mathrm{cm}^2$ at 6 keV that enables potential discovery of faint point sources.

For spatially extended emission, we need to treat the X-ray telescope's responses, such as the vignetting function and the point-spread functions including stray light, carefully. In a standard X-ray spectral analysis, we construct a so-called auxiliary response input file (`arf`), which describes the effective area of the telescope as a function of X-ray energy for an assumed spatial distribution of emission. To construct an `arf`, specific ray-tracing software of the telescope is required. Instead, we consider two `arfs` for extreme cases that are available, a point source at the optical axis and a flat field extending in a 5′ radius circle centered at the optical axis. In Figure 5, we display the effective area of XRISM/Resolve `arf` inputs for a point source and a 5′ radius flat field. For the foreground and background X-ray emission and the DM emission from the Galactic halo, the `arf` for a 5′ radius flat field is precise. However, for the DM emission from DGs, both `arfs` are not very precise. In our simulation, we adopt the flat-field `arf` *resolve_flt_spec_no(with)GV_20190611.arf*. In Section 4.4, we estimate the surface brightness of the DM emission corresponding to the projected upper limit of the spectral fit parameter. Assuming the spatial distribution of the DM emission expected for the Segue 1 DG, we estimate that the systematic error due to the choice of the `arf` in this conversion is less than ∼20%.

We simulate the diffuse X-ray background emission for XRISM/Resolve using the 5 eV resolution response input *resolve_h5ev_2019a.rmf*. We consider the model `TBabs*(APEC + bknpower + bknpower) + APEC` specified in XSPEC and simulate the spectra with the XRISM response using the `fakeit` routine. Here, `TBabs` models the ISM absorption in the Milky Way characterized by neutral hydrogen column density $n_{\mathrm{H}} = 1.8 \times 10^{20}\,\mathrm{cm}^{-2}$, the value of which we calculate for the Segue 1 line of sight according to the HI4PI map (HI4PI Collaboration et al. 2016). The first `APEC` component models for the Galactic hot gaseous halo and the double broken power-law components for the CXB, and the second `APEC` component models for the LHB and SWCX components. The DM signal model is constructed but not included in the background simulation. The parameters of these components are chosen as average values described in Section 3. We include the non-X-ray background in simulations by using the calibration input *resolve_h5ev_2019a_rslnxb.pha*.

We consider the telescope effective area for the flat field with and without the gate valve (GV) open using ancillary inputs *resolve_flt_spec_noGV_20190611.arf* and *resolve_flt_spec_withGV_20190611.arf*, respectively. The effective area for the flat field is generated with ray-tracing simulations assuming that the source of emission is uniformly distributed in the 5′ radius sky surrounding the telescope pointing direction. Correspondingly, the `DM` model is also computed for the 5′ radius sky area to account for a reference surface brightness value. In this way, any nonuniform telescope response to the photons emitted in the off-axis regions or outside of the field of view has been taken into account in our simulations. These considerations improve the accuracy of analysis compared to a point-source response. The difference in the effective area when the GV is open and closed is described in detail in M. Tsujimoto et al. (2018). We simulate a diffuse X-ray background for 100 ks, 5 Ms, and 100 Ms to compare the impact of exposure time. For each configuration, we generated 1000 realizations for both the photon background spectra and the non-X-ray background spectra. The non-X-ray backgrounds are subtracted later from the total diffuse background spectrum in the fitting procedure.

We also consider how sensitivity will improve for a future experiment with 2 eV energy resolution. For this, we constructed appropriate detector response inputs. The effective

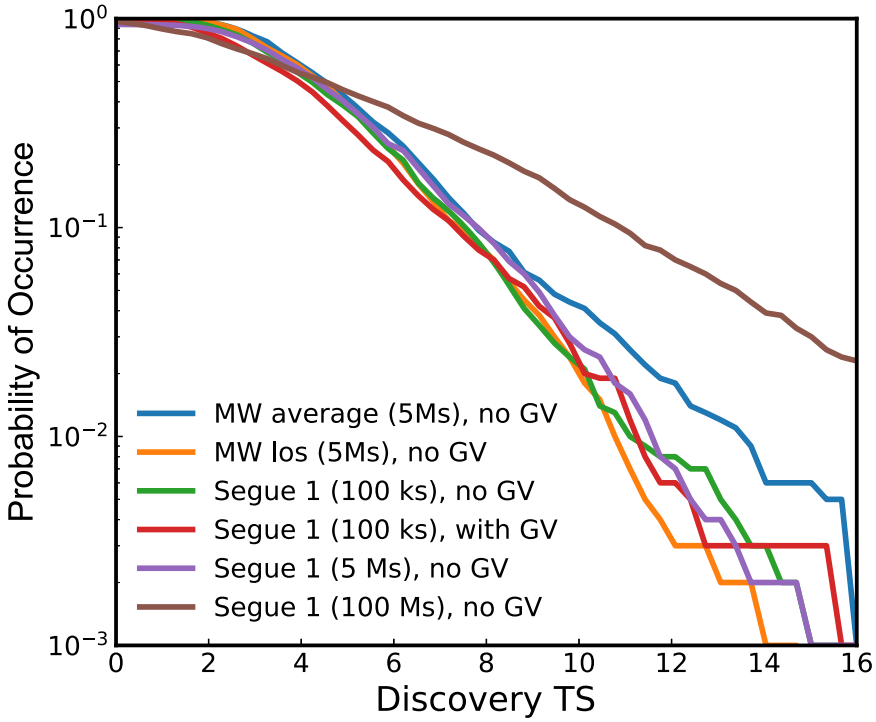

Figure 6. Probability of occurrence defined as p-values of the max $(C_0 - C_{\rm min})$ distribution for 1000 simulations. The $C_0 - C_{\rm min}$ values are computed for all fits with a DM signal model of different mass m_s in the searched energy range, the maximum of which is used as the global discovery TS.

area is assumed to have the same energy dependence as XRISM/Resolve, whose absolute amplitude is similar to an XRISM/Resolve point-source response of $\sim$300 cm^2 at 6 keV but about 8 times larger than the flat-field response of $\sim$40 cm^2 at 6 keV.

4.3. Analysis Fit

We fit the simulated data sets with the model TBabs*(APEC + bknpower + DM) + APEC in XSPEC. The hydrogen column density of the TBabs model is fixed at $n_{\rm H} = 1.8 \times 10^{20}$ cm^{-2}. The temperatures of the first and second APEC components are fixed at the average numbers that were used in the simulation, while the normalizations of both components are set as free fitting parameters. We use a single broken power law in the fit instead of the double broken power law in the simulations, because the low statistics of the simulation spectra do not allow one to constrain both power-law components. Therefore, we have only kept the first broken power law and only set the normalization as a free parameter for fitting. The DM component is the DM model signal, which is computed independently for each DM mass m_a as described in Section 2. We fitted for the DM signal in the range of 0.3–15 keV that is within the sensitive bandwidth of XRISM/Resolve. Normalization of the DM component is considered as a free parameter that is fitted to find upper limit projections constrained by the background spectrum.

In case the total photon count amount is low, we calculate the C-statistic (W. Cash 1979) instead of χ^2 as

$$C = 2\Sigma_{i=1}^{N}(tm_i) - S_i \ln(tm_i) + \ln(S_i!), \quad (11)$$

where S_i are the observed counts, t is the observation time, and m_i are the predicted count rates based on the considered model and detector response. The C-statistic is used to maximize the likelihood for the data following Poisson distribution. For each realization, we scan the DM normalization value starting from 0 to a sufficiently large number and find how the C-value depends on the normalization.

Since we are searching for the signal of DM χ with mass m_χ over a continuous energy range, in order to assess the significance of a local deviation from the background-only hypothesis, we need to also take into account the probability of such a deviation occurring anywhere within the search range, i.e., the "look elsewhere effect." Therefore, to investigate the distribution of the global discovery test statistic (TS), we have computed the C-value curves for different DM masses m_χ, i.e., signal energies centered around $m_\chi/2$, and found the maximum value of $(C_0 - C_{\rm min})$. We define $C_{\rm min}$ as the local minimum of the C-value reached in the normalization range of the scan and C_0 as the C-value where normalization equals 0. For all DM masses m_χ, the values of C_0 are identical, since they result from the same simulation data fitted with an identical diffuse X-ray background model. Thus, we use $\max(C_0 - C_{\rm min})$ to characterize the global discovery TS.

For all 1000 simulation data sets, we have performed the above analysis and obtained the distribution of the global discovery TS. The probability of occurrence of max $(C_0 - C_{\rm min})$ values, which is defined as the p-value of the $\max(C_0 - C_{\rm min})$ distribution, is shown in Figure 6. From the probability of occurrence curve $P(\max(C_0 - C_{\rm min}))$, we find the $\max(C_0 - C_{\rm min})$ value where $P = 2.5\%$, noted as C_Δ. In order to determine the global 95% confidence level sensitivity upper limit reach of DM normalization at each m_χ, we search for the minimum normalization value where $(C_{\rm min} + C_\Delta)$ is reached and compute the average for all simulations.

4.4. Sensitivity Forecast

The resulting sensitivity projections for decaying DM lifetime are shown in Figure 7 considering various observing

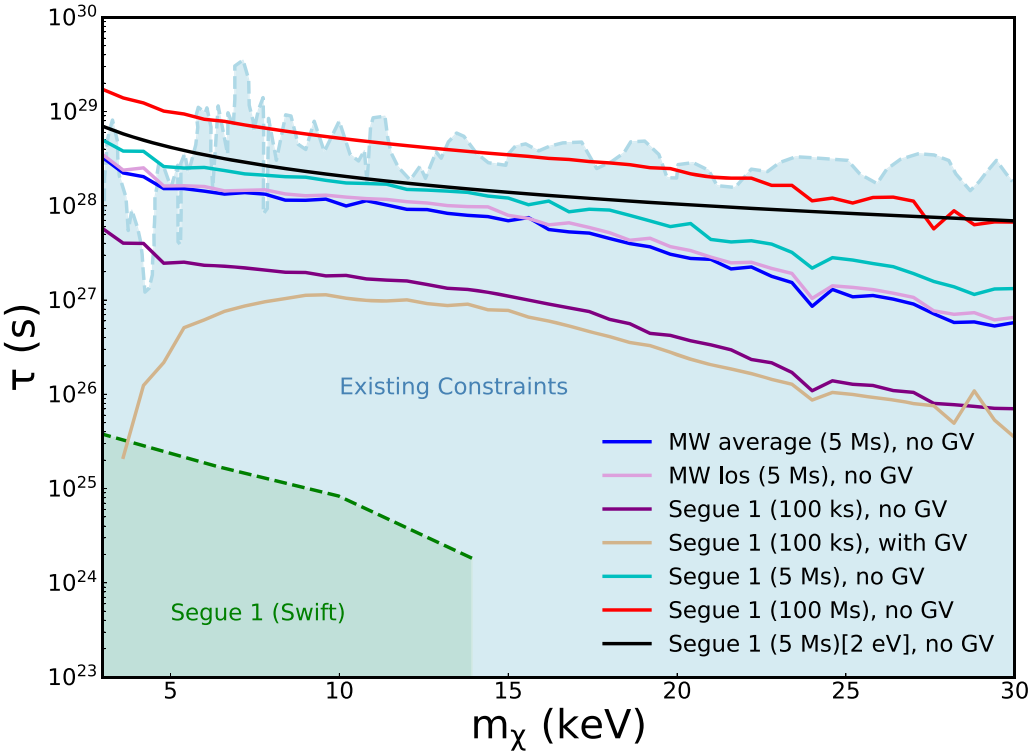

Figure 7. Sensitivity forecast for the lifetime of the decaying DM that can be probed by XRISM/Resolve considering various astrophysical target systems, exposures, and detector responses. Sensitivity curve from Milky Way DM halo for averaged random lines of sight and assuming GV open (blue), from Milky Way DM halo for the optimized line of sight and assuming GV open (pink), from Segue 1 line of sight assuming 100 ks observation with GV open (purple), from Segue 1 line of sight assuming 100 ks observation with GV closed (brown), from Segue 1 line of sight assuming 5 Ms observation with GV open (cyan), from Segue 1 line of sight assuming 100 Ms observation with GV closed (red), and from Segue 1 line of sight assuming 5 Ms observation with a hypothetical detector with 2 eV energy resolution and 8 times larger effective area than XRISM/Resolve with GV open (black). Combined existing constraints (blue shaded region) from S. Horiuchi et al. (2014), C. Dessert et al. (2020), B. M. Roach et al. (2020, 2023), and J. W. Foster et al. (2021) as well as constraints (green shaded region) derived from observations of Segue 1 by the Swift telescope (N. Mirabal 2010) are also shown.

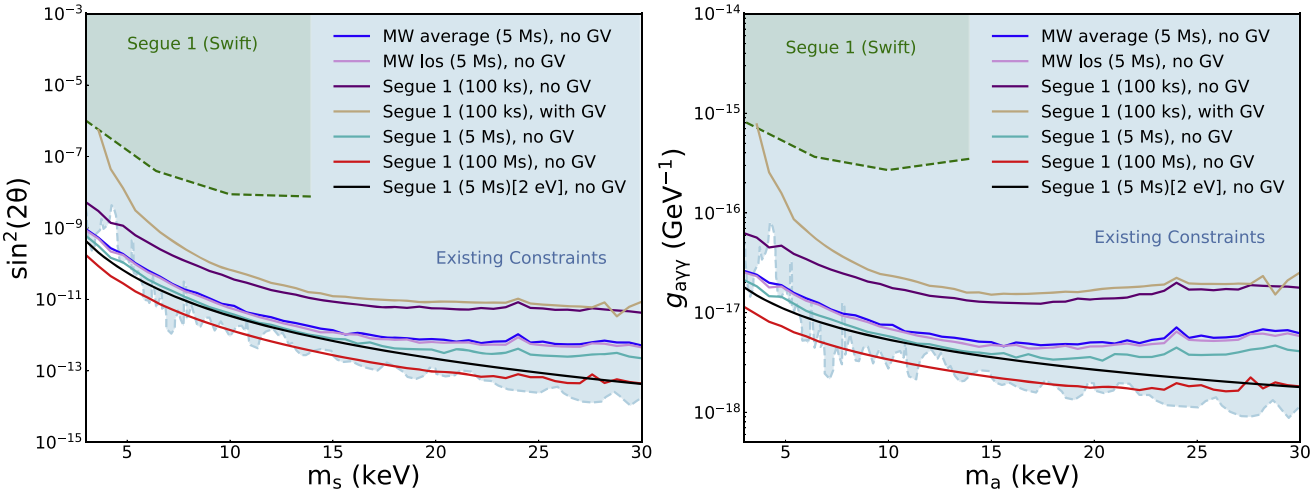

Figure 8. Sensitivity forecast for decaying DM that can be probed by XRISM/Resolve considering various astrophysical target systems, exposures, and detector responses. (Left) Parameter space for sterile neutrino sterile-active mixing angles. (Right) Parameter space for the ALP photon coupling coefficient. Constraints shown are analogous to Figure 7.

conditions including exposure times, GV configuration (open or closed), and astrophysical target systems. In Figure 8, we display sensitivity projections in terms of the sterile neutrino sterile-active mixing angle as well as the ALP photon coupling coefficient.

The fact that we used the `arf` response for the flat field may introduce systematic bias in the sensitivity forecast result, given that the DM in Segue 1 is more concentrated in the center region. We estimate that the surface brightness deviation caused by using the assumption of the flat-field `arf` response is

no more than 40%. As discussed in Section 2.2, the *D*-factors of the Galactic DM halo and Segue 1 DG are comparable. Namely, half of the DM emission along the Segue 1 line of sight is contributed from the Galactic DM halo, for which the flat-field response is appropriate. Therefore, overall, the systematic bias in the final result should be no more than 20%.

For the observation target systems, we have simulated the average of the random Galactic DM halo lines of sight, the optimized Galactic DM halo line of sight, and the line of sight toward Segue 1. For Segue 1, we compare the sensitivities obtained for 100 ks, 5 Ms, and 100 Ms exposures. GV configuration has a significant impact on the effective area, especially for energies below 2 keV. When the GV is closed, sensitivity below 2 keV is suppressed and the effective area decreases by 30% compared to when the GV is open (M. Tsujimoto et al. 2018). The sensitivity curves display dip features around energy of ∼12 keV, which is equivalent to a DM mass of ∼24 keV. This is mainly corresponding to the dip degradation in the effective area due to the Au absorption.

Intriguingly, our analysis demonstrates that with just 100 ks of observation, XRISM/Resolve can already improve on the previous Segue 1 DG decaying DM search using Swift data by approximately 2 orders of magnitude or more in sensitivity to DM coupling and decay time. Observations by XRISM/Resolve with an open GV enable probing decaying DM, especially with masses below 5 keV, with unprecedented sensitivity. Further, we have also analyzed the sensitivity of a hypothetical future detector assuming an energy resolution of 2 eV. Higher resolution and effective area enable better statistics, which improve the sensitivity primarily at higher energies and DM masses.

5. Faint Source Detection in Segue 1

Since XRISM/Xtend has a much larger field of view and better effective area than XRISM/Resolve,[8] it has a greater potential for discovering faint X-ray point sources. Hereafter, our discussion of simulations focuses on XRISM/Xtend.

Segue 1 is a fossil galaxy formed in the early Universe without substantial chemical evolution (A. Frebel et al. 2014). Exploring the population properties of the Segue 1 DG X-ray sources, such as their luminosity function, enables tracing back the formation of sources ∼1–10 Gyr earlier. According to the eROSITA all-sky survey point-source catalog (A. Merloni et al. 2024), there is an X-ray source located at R.A. $= 10^{h}06^{m}46\overset{s}{.}24$, decl. $= +16^{d}05^{m}46\overset{s}{.}02$, ∼4.′29 away from the Segue 1 center (i.e., R.A. $= 10^{h}07^{m}03\overset{s}{.}2$, decl. $= +16^{d}04^{m}25^{s}$), with a flux of 3.8×10^{-14} erg cm^{-2} s^{-1} in the 0.2–2.3 keV range. However, due to the limited exposure of the eROSITA observations, it is challenging to identify the energy spectrum of this point source or to establish if it is a member of an X-ray binary system associated with Segue 1. XRISM/Xtend's capabilities enable discovery of the underlying nature of the source with a longer exposure time.

We simulate the image and energy spectrum of the X-ray source in Segue 1 assuming a 100 ks observation of XRISM/Xtend and a spectral model using `TBabs*powerlaw` with $n_{\rm H} = 3.35 \times 10^{20}$ cm^{-2} and photon index PhoIndex = 1.7. We obtain about 800 net detector counts with a cumulative count rate of $\sim 6.8 \times 10^{-3}$ counts s^{-1} for this source. Performing a fit with the assumed model yields source parameters within a 12% error of the original assumed values. Fitting to the found simulation spectrum with a thermal bremsstrahlung model, we obtain the best-fit temperature of 11 ± 2 keV. This result is extremely high compared to the typical energy spectra of low-mass X-ray binary (LMXB) systems with high-energy roll-offs at ∼2 keV. Hence, such statistics enables investigating and constraining the true underlying nature of the faint X-ray point source. In particular, an LMXB and a background AGN can be clearly distinguished, while high-mass X-ray binary systems with high-energy roll-offs typically around ∼5–10 keV are marginally distinguishable from AGN.

No X-ray source has been detected within a 4′ field from the galaxy center of the Segue 1 galaxy at a flux threshold of 1×10^{-14} erg cm^{-2} s^{-1} for the 0.3–10 keV range. If there exists a faint X-ray source with a flux just below the eROSITA survey upper limit at the center of the Segue 1 galaxy, XRISM/Xtend can detect it with ∼140 counts considering a 100 ks observation. This is sufficient to distinguish the energy spectrum of the source, thus revealing crucial information for historic star formation activity in the central galactic region. In Figure 9, we display the image and a count distribution projected to a side view along the central pixels intersecting the detector plane that covers the presumed X-ray source region. The non-X-ray background and CXB are separately simulated using the calibration input *ah_sxi_pch_nx_full_20110530.pi* and the `Skyback` routine in `Heasim`. The log*N*–log*S* relation in the 0.3–10.0 keV range is specified according to in-depth observations (A. Moretti et al. 2003, 2009) for CXB modeling. As shown in Figure 9, the signal of the simulated point source is significantly higher than the non-X-ray background and CXB confusion limit.

Our analysis demonstrates that XRISM has unique opportunities of discovering new faint X-ray sources in the Segue 1 DG and shedding light on underlying historic star formation activity.

6. Conclusions

Sensitive X-ray observations of astrophysical systems, such as by the recently launched XRISM satellite mission, can reveal unique insights into the nature of DM as well as the identity of faint X-ray astrophysical sources. Employing dedicated simulations as well as background and foreground modeling, we comprehensively demonstrated that XRISM can probe decaying DM signatures, such as those from sterile neutrinos and ALPs, in the few to tens of keV mass range with unprecedented sensitivity.

We have identified optimal search strategies for decaying DM, including optimal lines of sight in the case of the Galactic DM halo, taking into account photon foreground emission from the Galactic hot gaseous halo. Among the DGs, we have identified Segue 1 as a particularly favorable observation target to explore decaying DM signatures considering the XRISM/Resolve field of view. The unique recession velocity and internal velocity dispersion of Segue 1 result in a distinctive DM signal along its line of sight, which is easily distinguishable from atomic emission lines. Our forecast analyses of sensitive decaying DM searches by XRISM/Resolve, performed under various assumptions, can be interpreted as new probes of sterile-active mixing angles for sterile neutrinos and axion–photon conversion coefficients for ALPs. We find that with just a 100 ks observation of Segue 1, XRISM/Resolve can probe the parameter space of decaying DM around two orders

[8] Further, XRISM/Xtend is not affected by the status of the GV.

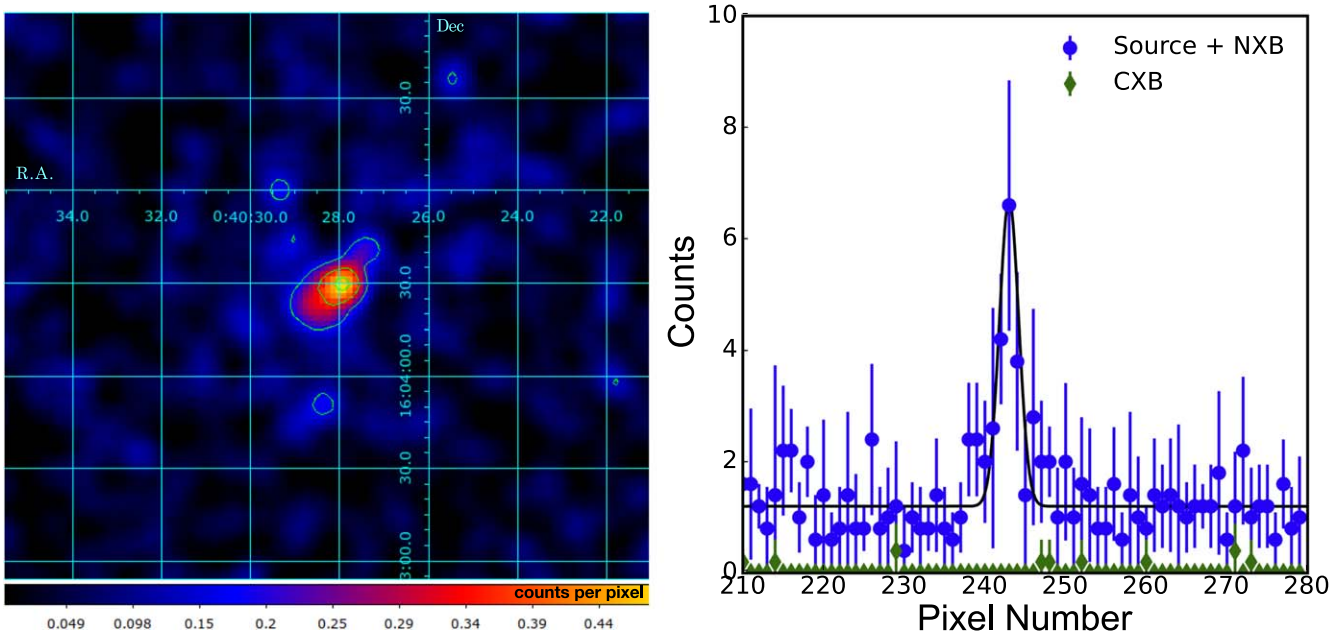

Figure 9. (Left) Simulated image of the point source with a flux set at the eROSITA all-sky survey detection threshold for an XRISM/Xtend 100 ks observation. (Right) Distribution of counts across the detector plane highlighting that the point-source counts are well distinguished from the non-X-ray background (baseline of the blue dots away from the peak) and the CXB contribution (green dots).

more sensitively than existing upper limits from Segue 1 established using data collected by the Swift telescope. Further, XRISM/Resolve offers powerful opportunities to probe the underexplored DM window around a few keV.

Further, we have established XRISM/Xtend's powerful capabilities for the discovery of faint X-ray point sources in Segue 1. We found that in-depth observations by XRISM can facilitate identifying the underlying astrophysical nature of these sources, providing valuable insights into the star-forming history of Segue 1.

Acknowledgments

This work was supported by the World Premier International Research Center Initiative (WPI), MEXT, Japan. V.T. acknowledges support from JSPS KAKENHI grant No. 23K13109, and K.M. acknowledges No. 20H05857. This work was performed in part at the Aspen Center for Physics, which is supported by the National Science Foundation grant PHY-2210452.

ORCID iDs

Yu Zhou https://orcid.org/0000-0002-5793-554X

References

Aharonian, F. A., Akamatsu, H., Akimoto, F., et al. 2017, ApJL, 837, L15
Anders, E., & Grevesse, N. 1989, GeCoA, 53, 197
Ando, S., Barik, S. K., Feng, Z., et al. 2021, PhRvD, 104, 023022
Arias, P., Cadamuro, D., Goodsell, M., et al. 2012, JCAP, 06, 013
Arnaud, K. A. 1996, in ASP Conf. Ser. 101, Astronomical Data Analysis Software and Systems V, ed. G. H. Jacoby & J. Barnes (San Francisco, CA: ASP), 17
Battaglia, G., Taibi, S., Thomas, G. F., & Fritz, T. K. 2022, A&A, 657, A54
Bertone, G., Hooper, D., & Silk, J. 2005, PhR, 405, 279
Boyarsky, A., Drewes, M., Lasserre, T., Mertens, S., & Ruchayskiy, O. 2019, PrPNP., 104, 1
Boyarsky, A., Ruchayskiy, O., Iakubovskyi, D., & Franse, J. 2014, PhRvL, 113, 251301
Bringmann, T., Depta, P. F., Hufnagel, M., et al. 2023, PhRvD, 107, L071702
Bulbul, E., Markevitch, M., Foster, A., et al. 2014, ApJ, 789, 13
Cappelluti, N., Li, Y., Ricarte, A., et al. 2017, ApJ, 837, 19
Cash, W. 1979, ApJ, 228, 939
Chen, M., Gelmini, G. B., Lu, P., & Takhistov, V. 2024, PhLB, 852, 138609
Chichiri, C., Gelmini, G. B., Lu, P., & Takhistov, V. 2022, JCAP, 09, 036
Cicuéndez, L., Battaglia, G., Irwin, M., et al. 2018, A&A, 609, A53
Collins, M. L. M., Read, J. I., Ibata, R. A., et al. 2021, MNRAS, 505, 5686
Collins, M. L. M., Tollerud, E. J., Rich, R. M., et al. 2020, MNRAS, 491, 3496
Cook, K. H., Mateo, M., Olszewski, E. W., et al. 1999, PASP, 111, 306
Crnojevic, D., Ferguson, A. M. N., Irwin, M. J., et al. 2014, MNRAS, 445, 3862
de Gouvea, A., Sen, M., Tangarife, W., & Zhang, Y. 2020, PhRvL, 124, 081802
Dehnen, W., McLaughlin, D. E., & Sachania, J. 2006, MNRAS, 369, 1688
Dessert, C., Ning, O., Rodd, N. L., & Safdi, B. R. 2024, PhRvL, 132, 211002
Dessert, C., Rodd, N. L., & Safdi, B. R. 2020, Sci, 367, 1465
Dodelson, S., & Widrow, L. M. 1994, PhRvL, 72, 17
Eby, J., & Takhistov, V. 2024, arXiv:2402.00100
Eilers, A.-C., Hogg, D. W., Rix, H.-W., & Ness, M. K. 2019, ApJ, 871, 120
Evans, N. W., Sanders, J. L., & Geringer-Sameth, A. 2016, PhRvD, 93, 103512
Fang, T., Bullock, J., & Boylan-Kolchin, M. 2013, ApJ, 762, 20
Farhang, A., van Loon, J. T., Khosroshahi, H. G., Javadi, A., & Bailey, M. 2019, NatAs, 3, 922
Foster, J. W., Kongsore, M., Dessert, C., et al. 2021, PhRvL, 127, 051101
Frebel, A., Simon, J. D., & Kirby, E. N. 2014, ApJ, 786, 74
Fukuda, Y., Hayakawa, T., Ichihara, E., et al. 1998, PhRvL, 81, 1562
Geha, M., Guhathakurta, P., Rich, R. M., & Cooper, M. C. 2006, AJ, 131, 332
Geha, M., van der Marel, R. P., Guhathakurta, P., et al. 2010, ApJ, 711, 361
Geha, M., Willman, B., Simon, J. D., et al. 2009, ApJ, 692, 1464
Gell-Mann, M., Ramond, P., & Slansky, R. 1979, arXiv:1306.4669
Gelmini, G. B., Kawasaki, M., Kusenko, A., Murai, K., & Takhistov, V. 2020a, JCAP, 09, 051
Gelmini, G. B., Kusenko, A., & Takhistov, V. 2021, JCAP, 06, 002
Gelmini, G. B., Lu, P., & Takhistov, V. 2019, JCAP, 12, 047
Gelmini, G. B., Lu, P., & Takhistov, V. 2020a, PhLB, 800, 135113
Gelmini, G. B., Lu, P., & Takhistov, V. 2020b, JCAP, 06, 008
Gelmini, G. B., Lu, P., & Takhistov, V. 2020c, JCAP, 2020, 008
Gupta, A., Mathur, S., Kingsbury, J., Das, S., & Krongold, Y. 2023, NatAs, 7, 799
Hagihara, T., Yao, Y., Yamasaki, N. Y., et al. 2010, PASJ, 62, 723
HI4PI Collaboration, Ben Bekhti, N., & Flöer, L. 2016, A&A, 594, A116
Higaki, T., Jeong, K. S., & Takahashi, F. 2014, PhLB, 733, 25
Higgs, C. R., & McConnachie, A. W. 2021, MNRAS, 506, 2766
Horiuchi, S., Humphrey, P. J., Onorbe, J., et al. 2014, PhRvD, 89, 025017

Jaeckel, J., Redondo, J., & Ringwald, A. 2014, PhRvD, 89, 103511
Ji, A. P., Koposov, S. E., Li, T. S., et al. 2021, ApJ, 921, 32
Kilbourne, C. A., Sawada, M., Tsujimoto, M., et al. 2018, PASJ, 70, 18
Koposov, S. E., Walker, M. G., Belokurov, V., et al. 2018, MNRAS, 479, 5343
Krivonos, R., Barinov, V., Mukhin, A., & Gorbunov, D. 2024, arXiv:2405.17861
Langhoff, K., Outmezguine, N. J., & Rodd, N. L. 2022, PhRvL, 129, 241101
Li, Y., & Bregman, J. 2017, ApJ, 849, 105
Liu, T., Merloni, A., Sanders, J., et al. 2024, ApJL, 967, L27
McCammon, D., & Sanders, W. T. 1990, ARA&A, 28, 657
McConnachie, A. W. 2012, AJ, 144, 4
Merloni, A., Lamer, G., Liu, T., et al. 2024, A&A, 682, A34
Minkowski, P. 1977, PhLB, 67, 421
Mirabal, N. 2010, MNRAS, 409, L128
Moretti, A., Campana, S., Lazzati, D., & Tagliaferri, G. 2003, ApJ, 588, 696
Moretti, A., Pagani, C., Cusumano, G., et al. 2009, A&A, 493, 501
Muñoz, R. R., Côté, P., Santana, F. A., et al. 2018, ApJ, 860, 66
Nakashima, S., Inoue, Y., Yamasaki, N., et al. 2018, ApJ, 862, 34
Navarro, J. F., Frenk, C. S., & White, S. D. M. 1996, ApJ, 462, 563
Ng, K. C. Y., Roach, B. M., Perez, K., et al. 2019, PhRvD, 99, 083005
Pal, P. B., & Wolfenstein, L. 1982, PhRvD, 25, 766
Perez, K., Ng, K. C. Y., Beacom, J. F., et al. 2017, PhRvD, 95, 123002
Predehl, P., Sunyaev, R. A., Becker, W., et al. 2020, Natur, 588, 227
Riemer-Sørensen, S., Wik, D., Madejski, G., et al. 2015, ApJ, 810, 48
Roach, B. M., Ng, K. C. Y., Perez, K., et al. 2020, PhRvD, 101, 103011
Roach, B. M., Rossland, S., Ng, K. C. Y., et al. 2023, PhRvD, 107, 023009
Sakai, K., Yao, Y., Mitsuda, K., et al. 2014, PASJ, 66, 83
Sekiya, N., Yamasaki, N. Y., & Mitsuda, K. 2016, PASJ, 68, S31
Shi, X., & Fuller, G. M. 1999, PhRvL, 82, 2832
Shrock, R. 1974, PhRvD, 9, 743
Snowden, S. L. 1993, AdSpR, 13, 103
Snowden, S. L., Egger, R., Freyberg, M. J., et al. 1997, ApJ, 485, 125
Tamura, T., Iizuka, R., Maeda, Y., Mitsuda, K., & Yamasaki, N. Y. 2015, PASJ, 67, 23
Tashiro, M., et al. 2018, Proc. SPIE, 10699, 106992
Tawa, N., Hayashida, K., Nagai, M., et al. 2008, PASJ, 60, S11
Torrealba, G., Koposov, S. E., Belokurov, V., & Irwin, M. 2016, MNRAS, 459, 2370
Tsujimoto, M., Okajima, T., Eckart, M. E., et al. 2018, PASJ, 70, 20
XRISM Science Team 2020, arXiv:2003.04962
Yanagida, T. 1979, Conf. Proc. C, 7902131, 95
Yao, Y., Shull, J. M., Wang, Q. D., & Cash, W. 2012, ApJ, 746, 166
Yao, Y., Wang, Q. D., Hagihara, T., et al. 2009, ApJ, 690, 143
Yoshino, T., Mitsuda, K., Yamasaki, N. Y., et al. 2009, PASJ, 61, 805
Zhou, Y., Mitsuda, K., & Yamasaki, N. Y. 2022, ApJ, 929, 128